NEUROSCIENCE

Distinct roles of parvalbumin and somatostatin interneurons in gating the synchronization of spike times in the neocortex

Hyun Jae Jang[1], Hyowon Chung[1], James M. Rowland[2], Blake A. Richards[3,4,5,6], Michael M. Kohl[2,7], Jeehyun Kwag[1]*

Synchronization of precise spike times across multiple neurons carries information about sensory stimuli. Inhibitory interneurons are suggested to promote this synchronization, but it is unclear whether distinct interneuron subtypes provide different contributions. To test this, we examined single-unit recordings from barrel cortex in vivo and used optogenetics to determine the contribution of parvalbumin (PV)– and somatostatin (SST)–positive interneurons to the synchronization of spike times across cortical layers. We found that PV interneurons preferentially promote the synchronization of spike times when instantaneous firing rates are low (<12 Hz), whereas SST interneurons preferentially promote the synchronization of spike times when instantaneous firing rates are high (>12 Hz). Furthermore, using a computational model, we demonstrate that these effects can be explained by PV and SST interneurons having preferential contributions to feedforward and feedback inhibition, respectively. Our findings demonstrate that distinct subtypes of inhibitory interneurons have frequency-selective roles in the spatiotemporal synchronization of precise spike times.

INTRODUCTION

Precisely timed spikes that are spatially coordinated or synchronized across multiple neurons with millisecond temporal precision have been shown to encode sensory information about stimuli (*1*–*3*). Information is contained in both the spike times (*2*, *4*) and the instantaneous firing rate (iFR) of precisely timed spike sequences (*1*, *3*), emphasizing the coexistence of temporal and rate codes during sensory information processing (*5*, *6*). Yet, the neural circuit mechanisms supporting the generation of highly synchronized spike sequences across cortical layers remain largely unknown. One potential mechanism for the spatiotemporal synchronization of precise spike times is inhibition. Theoretical as well as experimental studies have suggested that inhibition can modulate spatial correlation/synchronization of spike times between nearby neurons (*7*, *8*) and in neurons across multiple neuronal layers (*9*). The latency between excitation and inhibition (E/I latency) has been shown to modulate timing and rate of spike sequences in tandem in vivo (*5*, *6*). Thus, E/I latency may have a critical role in the spatiotemporal synchronization of spike times. Biologically, differences in E/I latency may be a result of distinct contributions from sensory-evoked feedforward (*10*, *11*) and feedback inhibition (*12*). Feedforward inhibition is recruited by afferent inputs that coactivate the inhibition and the neurons being inhibited, while feedback inhibition is recruited by activation of the same excitatory neurons that subsequently receive the inhibition. Hence, feedback inhibition has a slower onset latency than feedforward inhibition (*10*). Distinct subpopulations of cortical interneuron, such as parvalbumin (PV)– and somatostatin (SST)–positive inhibitory interneurons, are thought to provide distinct contributions to feedforward and feedback inhibition pathways, with perisomatic-targeting PV interneurons preferentially acting in a feedforward manner on excitatory neurons (*13*–*15*) and dendritic-targeting SST interneurons preferentially acting via feedback pathways to excitatory neurons (*14*, *15*). Together, we are presented with the following picture from the existing literature: Inhibition is important for spike-timing synchronization, and it is likely that feedforward and feedback inhibition control spatiotemporal spike-timing synchronization differently, depending on the iFR. At the same time, PV versus SST interneurons appear more involved in feedforward and feedback inhibition, respectively. Given these considerations, it is important to answer the following questions: (i) Do PV and SST interneurons make distinct contributions to the spatiotemporal synchronization of precise spike times? (ii) Are the contributions of PV and SST interneurons to spike-timing synchronization a function of the underlying iFR of the spike sequence? (iii) If any differences in the role of PV and SST interneurons in spike-timing synchronization exist, can they be ascribed to their distinct contributions to feedforward and feedback inhibition pathways in the neocortical microcircuit?

Here, we answer these three questions using in vivo single-unit recordings across all layers of the primary somatosensory cortex (S1). We find that the whisker-evoked spike times and their sequences are precisely synchronized between the granular layer (layer 4) and subgranular layers in subpopulation of neurons (layers 5 and 6). Using optogenetic perturbations of PV and SST interneurons, we demonstrate that both PV and SST interneurons promote the synchronization of precise spike times through these pathways, but with distinct contributions depending on the iFR [based on the interspike interval (ISI)] of the granular layer cells. Specifically, when the iFR is low (<12 Hz), PV interneurons are critical for precise spike-timing synchronization. In contrast, when the iFR is high (>12 Hz), SST interneurons are critical for precise spike-timing synchronization. Furthermore, using a computational model of spike-timing

[1]Department of Brain and Cognitive Engineering, Korea University, Seoul, Korea. [2]Department of Physiology, Anatomy and Genetics, University of Oxford, Oxford, UK. [3]Department of Biological Sciences, University of Toronto Scarborough, Toronto, Canada. [4]Mila, Montreal, QC, Canada. [5]Department of Neurology and Neurosurgery, McGill University, Montreal, QC, Canada. [6]School of Computer Science, McGill University, Montreal, QC, Canada. [7]Institute of Neuroscience and Psychology, University of Glasgow, Glasgow, UK.
*Corresponding author. Email: jkwag@korea.ac.kr

synchronization in a three-layered network with different levels of feedforward and feedback inhibition, we find that these results can be explained by a greater contribution to feedforward inhibition from PV interneurons and a greater contribution to feedback inhibition from SST interneurons. To our knowledge, our data provide the first ever direct evidence for a role of specialized inhibitory circuit motifs in the neocortex for the spatiotemporal synchronization of precise spike times. This may be critical to information processing in the neocortex.

RESULTS

Synchronization of whisker stimulation–evoked spike times between granular and subgranular layers

To investigate the synchronization of whisker stimulation–evoked spike times in vivo, we performed single-unit recordings from cortical layers (L) 2/3, 4, 5, and 6 in S1 of anesthetized mice using a 32-channel silicon probe while stimulating whiskers (Fig. 1A; see Materials and Methods). Recordings of single-unit activity were assigned to cortical layers using current source density (CSD) profiles (fig. S1) and DiI tracks of the silicon probe (Fig. 1B). On the basis of waveform asymmetry and spike width, we sorted the units into broad-spiking putative excitatory neurons and narrow-spiking putative inhibitory interneurons (Fig. 1C). Only spikes from putative excitatory neurons that showed whisker stimulation–evoked increase in firing rate in the peri-stimulus time histogram (PSTH) were used for further analysis (Fig. 1D; see Materials and Methods).

To determine the first layer that responds to whisker stimulation in S1, we analyzed the latency of the peak multiunit activity (MUA) of all whisker stimulation–responsive neurons in each layer (Fig. 1E; see Materials and Methods). The thalamo-recipient granular layer L4 had the earliest peak, followed closely by L2/3, and then after a longer delay subgranular L5 and L6, similar to what has been observed in other in vivo studies (*16*). This is consistent with the canonical feedforward neocortical microcircuit that has been previously proposed, where L4 is the major recipient of primary sensory information from the thalamus (*17*). However, the peak MUA latencies were heterogeneous across trials, and they were not statistically different [peak MUA latency of L2/3, 18.75 ± 3.71 ms; L4, 16.71 ± 3.37 ms; L5, 23.41 ± 6.31 ms; L6, 23.5 ± 5.74 ms; $F_{3,12} = 0.476$, $P = 0.71$, one-way analysis of variance (ANOVA) test] (Fig. 1E). This is indicative of noncanonical routes for information flow through cortical layers, for example, through direct connections between the thalamus and L5 (*18*). However, our investigation focused on the synchronization of whisker stimulation–evoked spike times between L4 and L5/L6, in line with the canonical model (*17*). Neurons in L2/3 were not included in our analyses due to limited statistical power resulting from a small number of detected L2/3 neurons, which may have been caused by the sparsity of L2/3 responses (*16*, *19*).

To better understand the synchronization of spike times between L4 and L5/L6, we performed a pairwise coherence analysis between spike-timing sequences of pairs of single putative excitatory neurons recorded during each whisker stimulation trial, with each pair composed of one neuron from L4 and one neuron from L5 or L6 (Fig. 1F). We developed a spike-time coherence score for each pair of L4-L5 and L4-L6 neurons (Fig. 1G). This spike-time coherence score measured the extent to which the L5/L6 neurons in the pair reproduced spike-timing sequences recorded in the L4 neuron during the whisker stimulation trial, allowing a synchronization time window of ±10 ms (gray shade, Fig. 1F). That is, this coherence score was the normalized cross-correlation of the two spike trains within the synchronization time window (±10 ms; see Materials and Methods), and if during whisker stimulation the L5 and L6 neurons in the pair tended to spike within the synchronization time window, the pair would receive a coherence score close to 1; otherwise, the pair would receive a coherence score close to 0 (Fig. 1, F and G).

When we examined spike-time coherence scores across all pairs and trials, the distributions were bimodal in both L4-L5 and L4-L6 pairs (L4-L5, $P < 0.001$; L4-L6, $P < 0.05$, Silverman's test with unimodal null hypothesis) (Fig. 1H, top and middle). In contrast, spike-time coherence scores between L4 spikes and spikes generated from a random Poisson process had a unimodal distribution ($P = 0.22$, Silverman's test with unimodal null hypothesis) (Fig. 1H, bottom). Moreover, in a surrogate dataset, bimodality of spike-time coherence scores disappeared when we shuffled ISI (fig. S2, A to C, top) or Poisson-randomized spike times (fig. S2, A to C, bottom). This suggests that in the real data, on any given trial, a subset of subgranular neurons do synchronize with L4 spike-timing sequences. We note that, on any given trial, different sets of neurons were more coherent or less coherent (fig. S3, A and D), suggesting that the bimodal distributions do not reflect the presence of two fundamentally distinct neuronal populations in the subgranular layers, consistent with previous in vivo observation that different synchronized groups may originate in the same or overlapping neuronal populations (*3*).

To focus the scope of our analysis onto those L5 and L6 neurons that synchronize with L4 spike times on any given trial, we fit a mixture of two log-normal distributions to the data using the expectation-maximization algorithm (see Materials and Methods). The data were well fit with this model [$r^2 = 0.93$ (L4-L5) and 0.85 (L4-L6)] (Fig. 1H) and provided us with an empirically determined threshold (Fig. 1H, vertical dotted line) for distinguishing between those neurons that participated in the synchronization of spike times from L4 that had spike-time coherence score greater than the threshold and those that did not [threshold = 0.10 (L5) and 0.11 (L6); see Materials and Methods] (Fig. 1, H and I). We refer to these neurons as "synchronized neurons" and "nonsynchronized neurons," respectively, but we note that the definition applied to neurons during individual trials, so a neuron could switch its status between synchronized and nonsynchronized across different trials (fig. S3A). In the analyses that follow, we only examine synchronized neurons.

Because spike time and firing rate coexist and are not completely dissociable in spike-timing sequences (*5*, *6*), it is important to examine how the synchronization of spike times depends on the iFR. Thus, we directly compared the spike times of synchronized L5 and L6 neurons with that of L4 neurons as a function of the L4 neurons' iFRs. To measure the similarity between spike times in pairs of L4-L5 and L4-L6 neurons at any given point in time and to express that as a function of the iFR, we used a previously developed spike-time similarity score that can be applied to sliding windows over time (see Materials and Methods) (*20*), and we then compared that to an estimate of the iFR in the L4 neurons. Specifically, at any point in time, we estimated the iFR of the L4 neuron in the pair as the inverse of the neuron's ISI (Fig. 1J). Then, we calculated the spike-time similarity score of the spikes in the L5/L6 neurons from the pair within the synchronization time window (±10 ms), providing an instantaneous similarity measure (iSR) (Fig. 1K). This measured the extent to which these synchronized L5 or L6 neurons were reproducing the spikes observed in the L4 neuron at each moment in

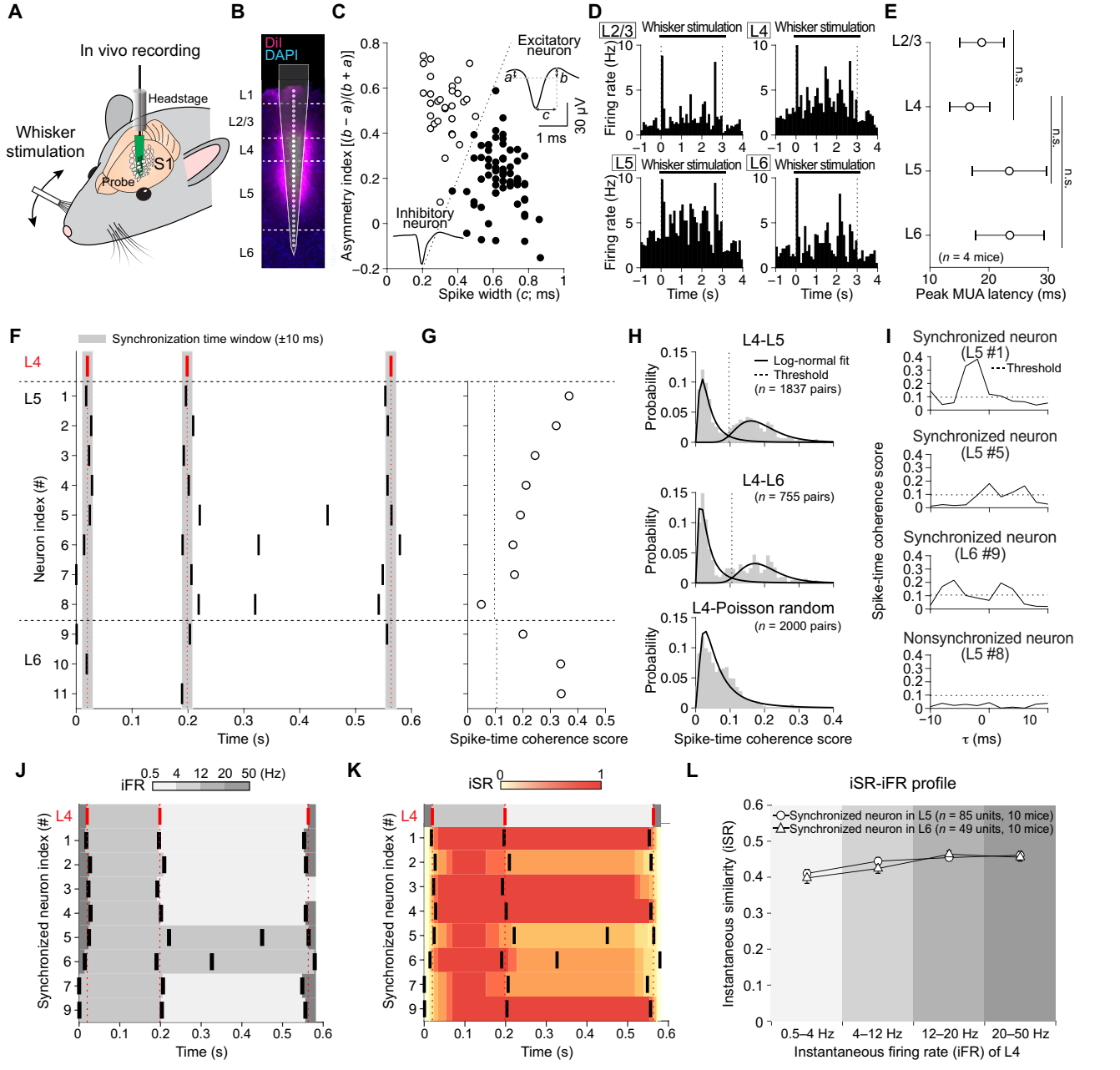

Fig. 1. Synchronization of whisker stimulation–evoked spike times between granular and subgranular layers in S1. (**A**) Electrophysiology recording in S1 during whisker stimulation in vivo. (**B**) Estimated location of the 32-channel silicon probe and contact sites in relation to cortical layers (magenta, DiI-stained probe track; blue, DAPI). (**C**) Spike waveform-based neuron classification in asymmetry index $[(b - a)/(b + a)]$ versus spike width (c). Dotted line, decision boundary. Inset: Initial baseline-to-peak amplitude (a), last baseline-to-peak amplitude (b), and spike width (c) of putative excitatory (filled circles) and inhibitory (empty circles) neurons. (**D**) Whisker stimulation–evoked changes in firing rate for four representative single units in layers (L) 2/3, 4, 5, and 6. Time point 0 denotes whisker stimulation onset. Black bar, whisker stimulation. (**E**) Peak latency of whisker stimulation–evoked multiunit activity (MUA) in L2/3, L4, L5, and L6 ($n = 4$ mice, n.s. $P > 0.05$, one-way ANOVA test). (**F**) Spike raster plot of putative excitatory neurons in L4, L5, and L6 from one recording trial during whisker stimulation. Gray shade indicates the synchronization time window (±10 ms). Red vertical dotted lines indicate spike times of L4 neurons. (**G**) Pairwise spike-time coherence scores of spike-timing sequences. Circles indicate pairwise coherence scores between a given neuron in L5 or L6 and the L4 neuron indicated in (F). Vertical dotted line represents the empirically defined threshold for classifying synchronized and nonsynchronized neurons [see (H) and (I)]. (**H**) Distribution of pairwise spike-time coherence scores of spike-timing sequences in pairs of L4-L5 (top; $n = 1837$ pairs from 10 mice), L4-L6 (middle; $n = 755$ pairs from 10 mice), and pairs of L4 and spikes generated from a random Poisson process (bottom; $n = 2000$ random spike pairs), fitted with log-normal distribution (solid curve). Threshold: Intersection between two log-normal distributions (vertical dotted line). (**I**) Representative spike-time coherence scores of neuron pairs in L4-L5 (top three panels) and L4-L6 (bottom panel) versus time lag (τ). Neurons with peak coherence scores above threshold (dotted line) are defined synchronized neuron or else nonsynchronized neuron. (**J**) Representative plot of iFR (0.5 to 4, 4 to 12, 12 to 20, and 20 to 50 Hz, gray color scale) of neurons in L4 and L5/L6. (**K**) Representative plot of iSR (maximum 1, red color scale) of neurons in L4 and L5/L6. (**L**) iSR-iFR profile of synchronized neurons in L5 (circle) and L6 (triangle). L5: $n = 85$ units and L6: $n = 49$ units recorded from 10 mice (n.s. $P > 0.05$, Wilcoxon rank sum test). All data are means ± SEM.

time (see Materials and Methods). As a result, for each time point, we had both an estimate of the iFR and a measure of the iSR in the L4-L5 and L4-L6 neuron pair. To simplify our analysis, we grouped the iFR into four different bins: 0.5 to 4, 4 to 12, 12 to 20, and 20 to 50 Hz. We selected these four bins as they correspond to the range of firing rates likely to be observed in vivo (*21*). We then plotted the iSR metric for each bin of iFRs, for each pair of L4-L5/L6 neurons (iSR-iFR profile; Fig. 1L). We found no evidence of a difference between pairs of L4-L5 and L4-L6 neurons in their iSR-iFR profiles (L5: $n = 85$ units, $F_{3,526} = 1.2$, $P = 0.31$; L6: $n = 49$ units, $F_{3,314} = 0.58$, $P = 0.63$, one-way ANOVA test) (Fig. 1L). Moreover, we found no evidence for differences in iSR at different iFR of L4 neurons (0.5 to 4 Hz, $P = 0.53$; 4 to 12 Hz, $P = 0.32$; 12 to 20 Hz, $P = 0.74$; 20 to 50 Hz, $P = 0.72$, Wilcoxon rank sum test) (Fig. 1L). Although the recorded neurons were sparse, a similar trend was observed in L2/3 (fig. S4), while such trend disappeared in the surrogate dataset (fig. S2, D and E). Together, these data demonstrate that, on any given trial, there are heterogeneous subsets of neurons in the subgranular layers that spatially synchronize spike-timing sequences between L4 and L5/L6 during whisker stimulation, but in a manner that does not differ between L5 and L6 and that is insensitive to the iFR of L4 neurons.

Optogenetic activation of PV and SST interneurons gates spike-timing synchronization

To investigate the role of inhibitory interneurons in the spatiotemporal synchronization of precise spike times, we optogenetically activated PV and SST interneurons via conditionally expressed Channelrhodopsin 2 (ChR2) with 473-nm blue light (*22*) during whisker stimulation (Fig. 2A). Immunostaining showed that ChR2-mCherry expressed across all cortical layers in PV-Cre (Fig. 2B, left) or SST-Cre mice (Fig. 2B, right). The ChR2 expression was confirmed by blue light stimulation–induced changes in the firing rate of putative excitatory neurons and PV or SST interneurons, as shown in the PSTH (Fig. 2, C and D). Optical stimulation of ChR2-expressing PV (ChR2-PV) and ChR2-expressing SST (ChR2-SST) interneurons increased their firing rates (Fig. 2, C and D, left), which, in turn, decreased the firing rates of some putative excitatory neurons (Fig. 2, C and D, right), confirming successful ChR2 expression. We chose three different blue light intensity levels (7.76, 39.47, and 78.52 mW/mm^2) that had no significant effect on the firing rates of putative excitatory neurons [standard deviation (SD) following activation of ChR2-PV interneurons in PV-Cre mice = 6.30%, SD following activation of ChR2-SST interneurons in SST-Cre mice = 6.86%; see Materials and Methods] (fig. S5, A to D) and confirmed that blue light could activate ChR2 in subgranular layers (fig. S6A).

Optical activation of ChR2-PV or ChR2-SST interneurons during whisker stimulation did not interfere with the generation of reliable whisker stimulation–evoked responses in L4 (Fig. 2, E and F, top) and L5/L6 (Fig. 2, E and F, bottom). Hence, we were still able to examine spike-time coherence scores of putative excitatory neurons in L5 and L6 during optical activation of ChR2-PV and ChR2-SST interneurons (Fig. 2, G and H). The bimodal distribution of spike-time coherence scores was not significantly affected in pairs of L4-L5 neurons (ChR2-PV in L4-L5, $P = 0.89$; ChR2-SST in L4-L5, $P = 0.24$, Kolmogorov-Smirnov test) (Fig. 2, G and H, top) and L4-L6 neurons (ChR2-PV in L4-L6, $P = 0.77$; ChR2-SST in L4-L6, $P = 0.05$, Kolmogorov-Smirnov test) (Fig. 2, G and H bottom). These data demonstrate that activation of PV and SST interneurons generally does not have an impact on the switching between synchronous and nonsynchronous mode of synchronized neurons over each trial (fig. S3, B to D). Next, we examined whether the effect of PV and SST interneuron activation on spike-timing synchronization could be dependent on the iFR (Fig. 2, I and J). We found very pronounced effects of optical activation of ChR2-PV and ChR2-SST interneurons on the iSR-iFR profiles. Specifically, optical activation of ChR2-PV interneurons led to a large decrease in the iSR measures of both L5 ($n = 66$ units; 12 to 20 Hz, $P < 0.001$; 20 to 50 Hz, $P < 0.001$, Wilcoxon rank sum test) and L6 excitatory neurons ($n = 26$ units; 12 to 20 Hz, $P < 0.001$; 20 to 50 Hz, $P < 0.001$, Wilcoxon rank-sum test) at high iFR (Fig. 2K). In contrast, optical activation of ChR2-SST interneurons led to pronounced decreases in the iSR measures of both L5 ($n = 46$ units; 0.5 to 4 Hz, $P < 0.001$; 4 to 12 Hz, $P < 0.001$, Wilcoxon rank sum test) and L6 ($n = 31$ units; 0.5 to 4 Hz, $P < 0.001$; 4 to 12 Hz, $P < 0.001$, Wilcoxon rank-sum test) at low iFR (Fig. 2L). It is possible that different light stimulation intensities used in optical manipulations of ChR2-PV and ChR2-SST interneurons cause distinct perturbations in the neural circuit (*23*, *24*). However, we found that the iSR-iFR profiles were robust for different light stimulation intensities used (fig. S7, A and B). To further see whether different levels of perturbations in L5/L6 excitatory neurons' activity caused by optogenetic manipulations had any effect on the iSR-iFR profiles, we analyzed the different perturbation levels as change in firing rates of L5/L6 excitatory neurons before and during optical manipulations in each unit ($FR_{light\ on}/FR_{light\ off}$; fig. S8) and plotted the iSR-iFR profiles according to three different bins of perturbation levels. We found that the iSR-iFR profiles were also unaffected for different perturbation levels (fig. S8, A and B), indicating that optogenetic manipulations of PV and SST interneurons on iSR-iFR profiles can be generalized for different levels of neural circuit perturbations. The complementary effects of PV and SST interneurons on the iSR-iFR profiles of L5 and L6 putative excitatory neurons suggest that these different classes of inhibitory interneurons act as iFR-selective gates, with PV interneurons gating spike-timing synchronization when L4 neurons are active with high iFR (i.e., acting as a low-pass filter) and SST interneurons gating spike-timing synchronization when L4 neurons are quiet with low iFR (i.e., acting as a high-pass filter). These results demonstrate that PV and SST interneurons do exert strong, complementary influences on the synchronization of spike-timing sequences from granular to the subgranular layers.

Optogenetic silencing of PV and SST interneurons promotes spike-timing synchronization

Our optical activation data demonstrated that PV and SST interneurons can gate spike-timing synchronization at specific iFRs. We hypothesized that these interneurons might also promote spike-timing synchronization in the range of the iFR that they do not gate. In other words, we speculated that if PV interneurons gate spike times at high iFR, then they may promote spike-timing synchronization at low iFR, and vice versa for SST interneurons. To test this hypothesis, we optogenetically silenced PV and SST interneurons using Archaerhodopsin-3 (Arch) (*25*) with 565-nm green light (Fig. 3A). Immunostaining showed Arch-EYFP (enhanced yellow fluorescent protein) expressed across all cortical layers in PV-Cre or SST-Cre mice (Fig. 3B). Illumination of Arch-expressing PV (Arch-PV) and Arch-expressing SST (Arch-SST) interneurons decreased their firing rates (Fig. 3, C and D, left), which, in turn, increased the firing rates of some putative excitatory neurons (Fig. 3, C and D, right),

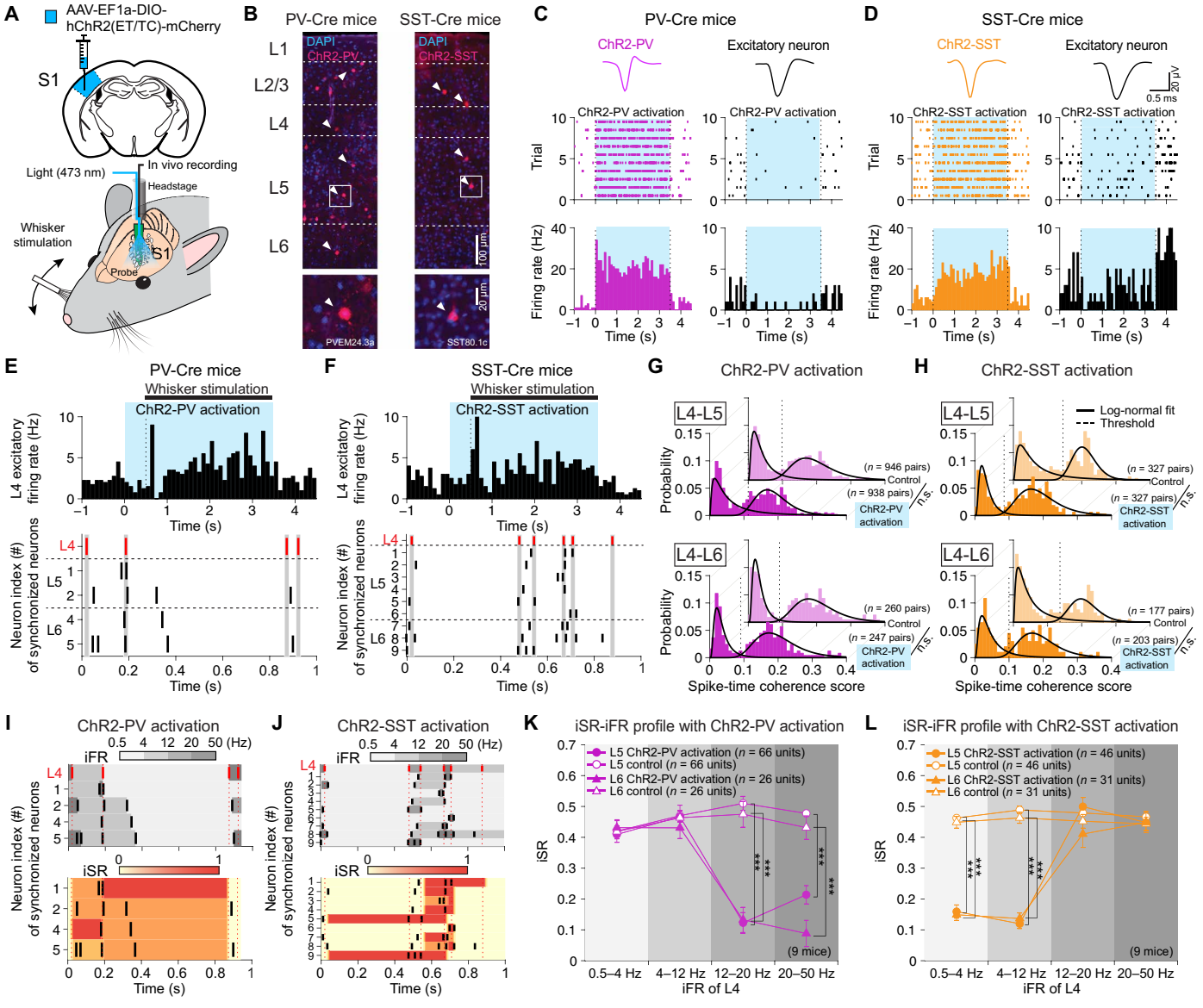

Fig. 2. Optogenetic activation of PV and SST interneurons gates the synchronization of spike times in a frequency-selective manner. (**A**) Top: Schematic of the injection of AAV-EF1a-DIO-hChR2(ET/TC)-mCherry (ChR2, blue) into S1. Bottom: Electrophysiology recording during whisker stimulation and blue light stimulation (473 nm) in either PV-Cre or SST-Cre mice. (**B**) ChR2-mCherry–expressing PV (ChR2-PV) interneurons in PV-Cre mice (red, left) and ChR2-mCherry–expressing SST (ChR2-SST) interneurons in SST-Cre mice (red, right) among all cells stained with DAPI (blue). (**C**) Representative spike waveforms (top), raster plots (middle), and peri-stimulus time histograms (PSTH; bottom) of putative ChR2-PV interneuron (magenta, left) and excitatory neuron (black, right) during blue light stimulation (3.5 s; blue shade) in PV-Cre mice. (**D**) Same as (C) but for putative ChR2-SST interneuron (orange) in SST-Cre mice. (**E** and **F**) PSTHs of putative L4 excitatory neurons (top) and the spike raster plots (bottom) of synchronized neurons in L5 and L6 during whisker stimulation (black horizontal bar) with blue light stimulation (blue shade) in PV-Cre mice (E) and SST-Cre mice (F). Light stimulation preceded whisker stimulation by 500 ms (vertical dotted lines; top). Gray shade indicates the synchronization time window (±10 ms). Red vertical dotted lines indicate the spike times of L4 neurons. (**G** and **H**) Distribution of pairwise spike-time coherence scores of neuron pairs in L4-L5 (top; control in PV-Cre mice, 946 pairs; ChR2-PV activation, 938 pairs from nine mice; control in SST-Cre mice, 327 pairs; ChR2-SST activation, 327 pairs from nine mice) and L4-L6 (bottom; control in PV-Cre mice, 260 pairs; ChR2-PV activation, 247 pairs from nine mice; control in SST-Cre mice, 177 pairs; ChR2-SST activation, 203 pairs from nine mice) with ChR2-PV activation (G, magenta) and ChR2-SST activation (H, orange) and in control (light magenta/orange), fitted with log-normal distribution (solid curve). Vertical dotted line: Threshold between synchronized and nonsynchronized neurons (n.s. $P > 0.05$, Kolmogorov-Smirnov test). (**I** and **J**) Representative plot of iFR (four bins: 0.5 to 4, 4 to 12, 12 to 20, and 20 to 50 Hz, gray color scale; top) and iSR (maximum 1, red color scale; bottom) of neurons in L4 and L5/L6 during blue light stimulation in PV-Cre mice (I) and SST-Cre mice (J). Red vertical dotted lines indicate the spike times of the L4 neurons. (**K** and **L**) iSR-iFR profiles of synchronized neurons in L5 (circle) and L6 (triangle) during blue light on (filled) and off (empty) in PV-Cre mice (K, magenta; L5, $n = 66$ units; L6, $n = 26$ units; nine mice) and in SST-Cre mice (L, orange; L5, $n = 46$ units; L6, $n = 31$ units; nine mice). All data are means ± SEM. The number of animals and the isolated single-units are as indicated (***$P < 0.001$, Wilcoxon rank sum test).

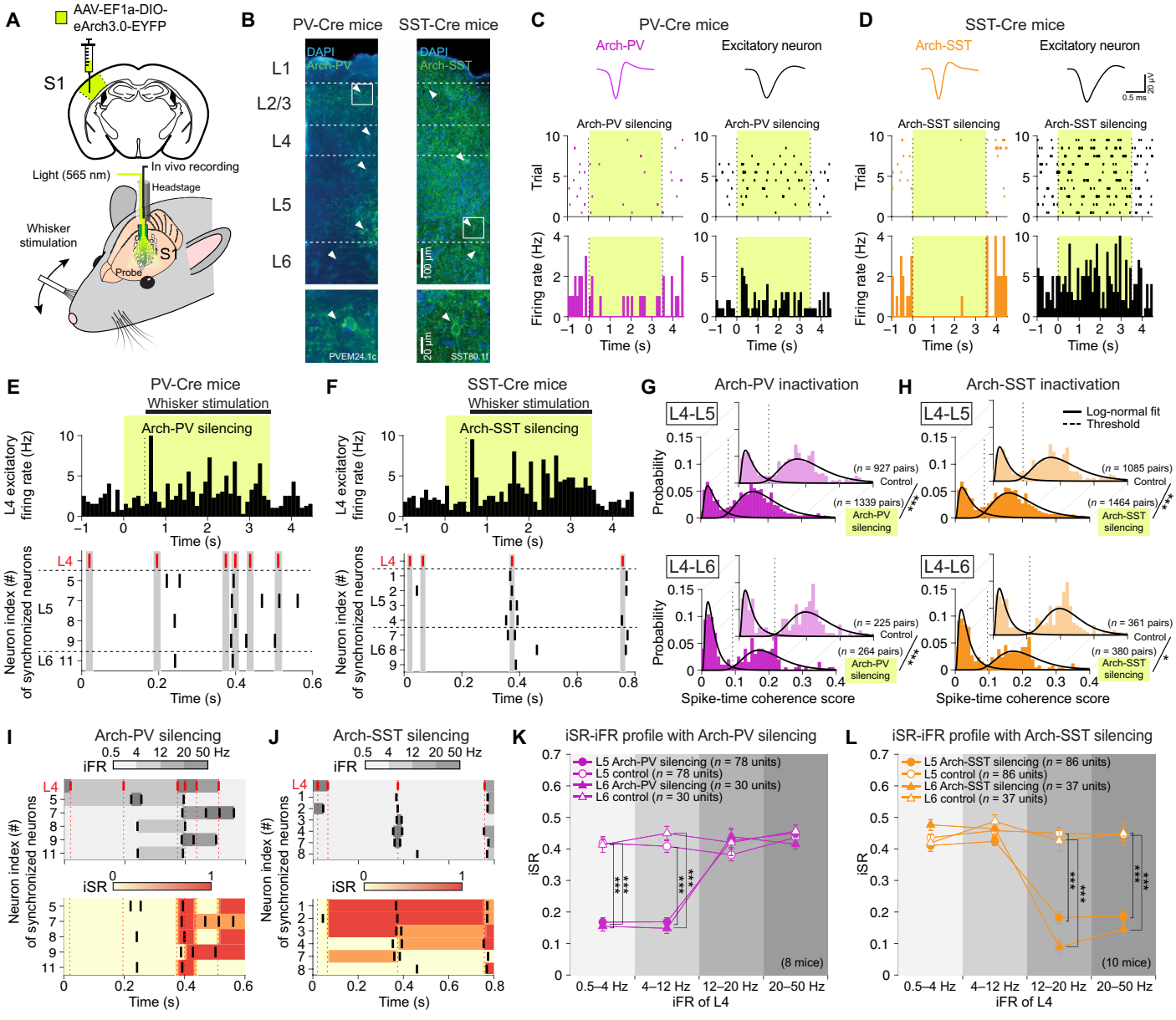

Fig. 3. Optogenetic silencing of PV and SST interneurons promotes the synchronization of spike times in a frequency-selective manner. (**A**) Top: Schematic of the injection of AAV-EF1a-DIO-eArch3.0-EYFP (Arch; green) into S1. Bottom: Electrophysiology recording during whisker stimulation and green light stimulation (565 nm) in either PV-Cre or SST-Cre mice. (**B**) Arch-EYFP–expressing PV interneurons (Arch-PV) in PV-Cre mice (green, left) and Arch-EYFP–expressing SST interneurons (Arch-SST) in SST-Cre mice (green, right) in EYFP among all cells stained with DAPI (blue). (**C**) Representative spike waveforms (top), raster plots (middle), and PSTHs (bottom) of putative Arch-PV interneuron (magenta, left) and excitatory neuron (black, right) during green light stimulation (3.5 s; green shade) in PV-Cre mice. (**D**) Same as (C) but for putative Arch-SST interneuron (orange) in SST-Cre mice. (**E** and **F**) PSTHs of putative L4 excitatory neurons (top) and the raster plots (bottom) of synchronized neurons in L5 and L6 during whisker stimulation (black horizontal bar) with green light stimulation (green shade) in PV-Cre mice (E) and SST-Cre mice (F). Light stimulation preceded whisker stimulation by 500 ms (vertical dotted lines; top). Gray shade indicates the synchronization time window (±10 ms). Red vertical dotted lines indicate the spike times of L4 neurons. (**G** and **H**) Distribution of pairwise spike-time coherence scores of neuron pairs in L4-L5 (top; control in PV-Cre mice, 927 pairs; Arch-PV silencing, 1339 pairs from 8 mice; control in SST-Cre mice, 1085 pairs; Arch-SST silencing, 1464 pairs from 10 mice) and L4-L6 (bottom; control in PV-Cre mice, 225 pairs; Arch-PV silencing, 264 pairs from 8 mice; control in SST-Cre mice, 361 pairs; Arch-SST silencing, 380 pairs from 10 mice) with Arch-PV silencing (G, magenta) and Arch-SST silencing (H, orange) and in control (light magenta/orange), fitted with log-normal distribution (solid curve). Vertical dotted line: Threshold between synchronized and nonsynchronized neurons (*$P < 0.05$ and ***$P < 0.001$, Kolmogorov-Smirnov test). (**I** and **J**) Representative plot of iFR (four bins: 0.5 to 4, 4 to 12, 12 to 20, and 20 to 50 Hz, gray color scale; top) and iSR (maximum 1, red color scale; bottom) of neurons in L4 and L5/L6 during green light stimulation in PV-Cre mice (I) and SST-Cre mice (J). Red vertical dotted lines indicate the spike times of the L4 neurons. (**K** and **L**) iSR-iFR profiles of synchronized neurons in L5 (circle) and L6 (triangle) during green light on (filled) and off (empty) in PV-Cre mice (K, magenta; L5, $n = 78$ units; L6, $n = 30$ units; 8 mice) and in SST-Cre mice (L, orange; L5, $n = 86$ units; L6, $n = 37$ units; 10 mice). All data are means ± SEM. The number of animals and the isolated single units are as indicated (***$P < 0.001$, Wilcoxon rank-sum test).

confirming successful Arch expression and activation. We selected three different light intensity levels (2.69, 5.05, and 19.07 mW/mm^2) that had no significant effect on the firing rates of putative excitatory neurons (SD following Arch-PV in PV-Cre mice = 6.35%, Arch-SST in SST-Cre mice = 6.31%; see Materials and Methods) (fig. S5, E to H), and we confirmed that green light could activate Arch in subgranular layers (fig. S6B).

Optical silencing of Arch-PV and Arch-SST interneurons did not affect the generation of reliable, whisker stimulation–evoked responses in L4 (Fig. 3, E and F, top) and L5/L6 (Fig. 3, E and F, bottom), allowing us to again examine spike-time coherence scores. Unlike in the case of optical activation of these interneuron classes, we found a moderate change in the spike-time coherence scores between L4-L5 pairs during optical silencing of Arch-PV and Arch-SST interneurons (Arch-PV, $P < 0.001$; Arch-SST, $P < 0.001$, Kolmogorov-Smirnov test) and L4-L6 pairs during optical silencing of Arch-PV and Arch-SST interneurons (Arch-PV, $P < 0.001$; Arch-SST, $P < 0.05$, Kolmogorov-Smirnov test) (Fig. 3, G and H). In addition, the spike-time coherence score distributions analyzed only for synchronized neurons revealed that silencing of Arch-PV and Arch-SST interneurons had significant effects (Arch-PV in L4-L5, $P < 0.001$; Arch-SST in L4-L5, $P < 0.001$; Arch-PV in L4-L6, $P < 0.01$; Arch-SST in L4-L6, $P < 0.001$, Kolmogorov-Smirnov test) (Fig. 3, G and H), implying that PV and SST interneurons might promote the synchronization of precise spike times by modulating synchronized neurons, while overall probability of a neuron switching between synchronous and nonsynchronous mode is unaffected by optogenetic silencing over each trial (fig. S3, B to D). Next, we again examined the iSR-iFR profiles for L5 and L6 neurons in light-on versus light-off conditions (Fig. 3, I and J). We found that optical silencing of PV interneurons led to a selective decrease in the iSR measures of both L5 ($n = 78$ units; 0.5 to 4 Hz, $P < 0.001$; 4 to 12 Hz, $P < 0.001$, Wilcoxon rank-sum test) and L6 excitatory neurons ($n = 30$ units; 0.5 to 4 Hz, $P < 0.001$; 4 to 12 Hz, $P < 0.001$, Wilcoxon rank-sum test) at low iFR (Fig. 3K). In contrast, optical silencing of SST interneurons selectively decreased the iSR measures of both L5 ($n = 86$ units; 12 to 20 Hz, $P < 0.01$; 20 to 50 Hz, $P < 0.001$, Wilcoxon rank sum test) and L6 ($n = 37$ units; 12 to 20 Hz, $P < 0.001$; 20 to 50 Hz. $P < 0.001$, Wilcoxon rank sum test) at high iFR (Fig 3L). iSR-iFR profiles were also robust for the three different light stimulation intensities used for optogenetic silencing of Arch-PV and Arch-SST interneurons (fig. S7, C and D) and for different levels of perturbations in L5/L6 excitatory neurons (fig. S8, C and D), indicating that these results could also be generalized for different levels of neural circuit perturbations. These findings supported our hypothesis, demonstrating that PV and SST interneurons not only gate the synchronization of spike-timing sequences but also promote it, though at different and complementary iFRs. Specifically, PV interneurons gate spike-timing synchronization at high firing rates and promote it at low firing rates, whereas SST interneurons gate spike-timing synchronization at low firing rates and promote it at high firing rates.

Preferential recruitment of feedforward and feedback inhibition explains the frequency-selective synchronization of spike times by PV and SST interneurons

One hypothesis as to why PV and SST interneurons have these distinct, complementary effects on spike-timing synchronization is that they contribute differentially to feedforward versus feedback inhibition pathways (*13*–*15*). However, there is as of yet no experimental technique that can selectively activate or silence feedforward and feedback inhibition pathways in vivo. Therefore, to address this question, we built a three-layer spiking excitatory neural network model of the sort that has previously been used in studies on the synchronization of precise spike times (see Materials and Methods for more details on the computational model) (*26*, *27*). With this model, we could directly implement two distinct inhibitory neural circuit motifs, e.g., feedforward and feedback inhibition motifs (Fig. 4A). Furthermore, we could measure iSR-iFR profiles in our in silico model and directly compare them to our in vivo data under various conditions of optogenetic perturbation. To calculate iSR-iFR profiles for the in silico model, we randomly selected synchronized spike-timing sequences recorded from putative excitatory neurons in L4 during whisker stimulation. We fed these sequences as inputs to the spiking neural network model and examined spike-timing sequences that were synchronized to the final layer of the model (Fig. 4B). We then calculated the synthetic iSR-iFR profiles by treating the input layer (L_{INPUT}) as the functional equivalent to granular layer in S1 and measuring the spike-time similarity scores for neurons in the output layer of the model (L3), treating them as the functional equivalent to subgranular neurons. Thus, for every pair of L_{INPUT}-L3 neurons in the network model, we could calculate an iSR-iFR profile, much as we did for L4 and L5/L6 neurons in S1 (Fig. 4, C and D). As we varied the ratio of feedforward and feedback inhibition, we found that, in the model with a 7:3 mixture of feedforward and feedback inhibition, spike sequences were synchronized across all iFR ranges (Fig. 4, A to E). Using this network model with both feedforward and feedback inhibition circuit motifs present, we investigated whether perturbing the feedforward or feedback circuit motifs could be related to the optical manipulations of PV and SST interneurons as in Figs. 2 and 3. We could not directly simulate optogenetic inputs to the neurons, because (i) we do not know exactly how much current our cells received when the opsins were activated, and (ii) our model is a phenomenological model that does not fully capture interneuron interactions and the way in which silencing one population of interneurons may affect another. Therefore, to model a change in the balance between feedforward and feedback inhibition, we manipulated the synaptic weights to the inhibitory neurons in a bidirectional manner. Specifically, when the synaptic weights of feedforward inhibition (W_{FFI}) were increased ($\Delta W_{FFI} > 0$), this was complemented by a decrease in the synaptic weights of feedback inhibition ($\Delta W_{FBI} < 0$) to balance the total amount of inhibition in the model (Fig. 4F). When we did this, shifting the balance to feedforward inhibition in the model, precise spike times synchronized at low iFRs (Fig. 4, F to H), as we had observed during optical activation of ChR2-PV interneurons and optical silencing of Arch-SST interneurons (Fig. 2K and 3L). Treating the in silico and in vivo iSR-iFR profiles as four-dimensional Euclidean vectors, we measured the Euclidean similarity between them and found that the iSR-iFR profiles in the network model with increased W_{FFI} ($\Delta W_{FFI} > 0$), which was complemented by a decrease in ΔW_{FBI} ($\Delta W_{FBI} < 0$), were similar to the optical activation of ChR2-PV interneurons and optical silencing of Arch-SST interneurons (Fig. 4I). In contrast, when ΔW_{FBI} was increased ($\Delta W_{FBI} > 0$), which was complemented by a decrease in ΔW_{FFI} ($\Delta W_{FFI} < 0$) to balance the total amount of inhibition in the network, we found that spike times synchronized at high iFRs (Fig. 4, J to L), as we had observed during optical activation of ChR2-SST interneurons and optical silencing of Arch-PV interneurons (Figs. 2L and 3K). Similarly, the

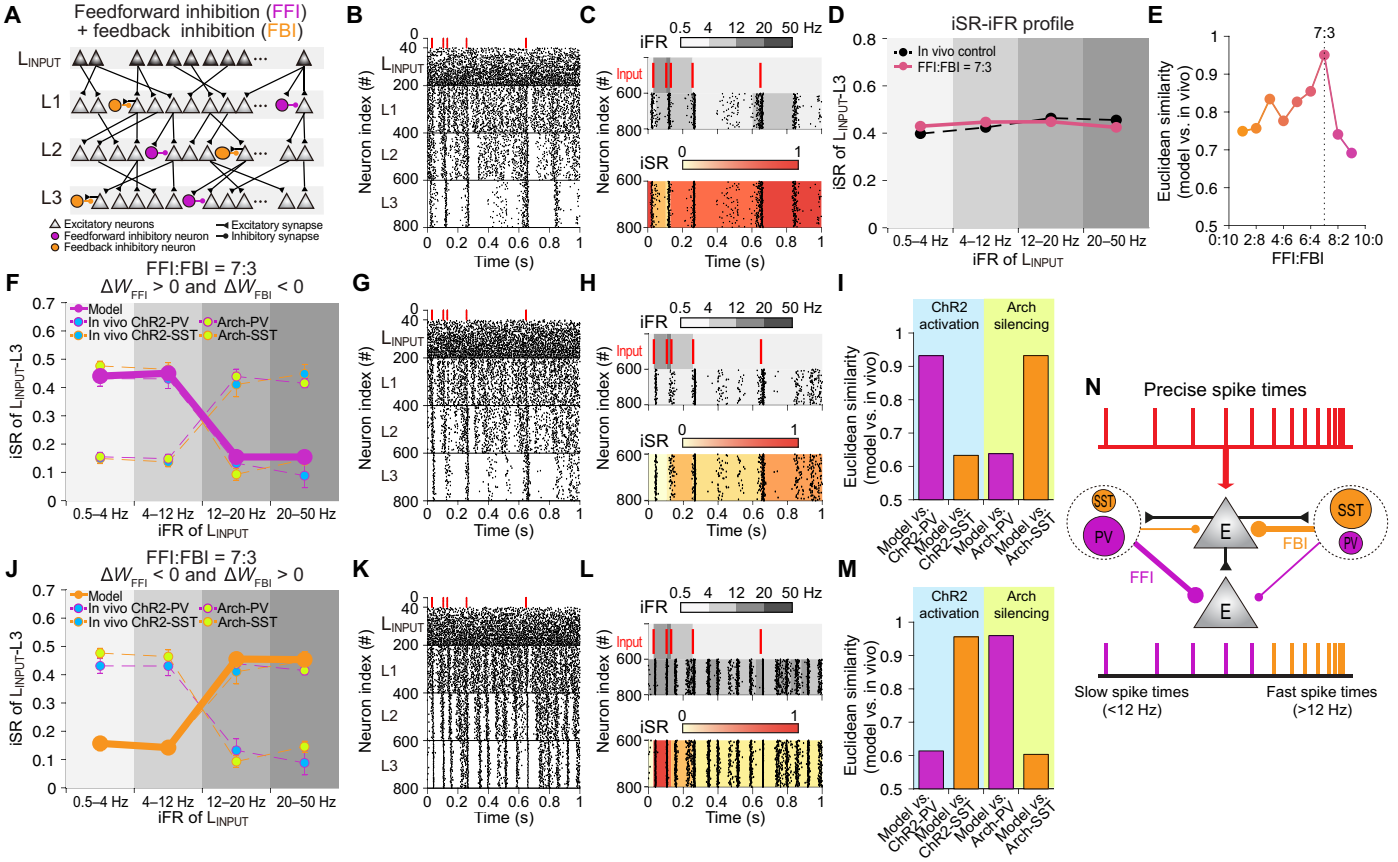

Fig. 4. PV and SST interneurons preferentially recruit feedforward and feedback inhibition for frequency-selective gating of spike-timing synchronization. (**A**) Schematic of a three-layer network model consisting of 200 single-compartment Hodgkin-Huxley excitatory neuron models (triangles) and 50 inhibitory interneuron models (circles) that provide feedforward inhibition (FFI; magenta) and feedback inhibition (FBI; orange) at 7:3 ratio. (**B**) Spike raster plot of the model in response to spike-timing sequence recorded in granular layer in S1 in vivo (red). Dots indicate spikes. A subset of neurons (40 neurons) in the input layer (L_{INPUT}) received the input (red dots), while the rest spiked spontaneously (black dots), reflecting sparseness. (**C**) Representatives of iFR (four bins: 0.5 to 4, 4 to 12, 12 to 20, and 20 to 50 Hz, gray color scale; top) and iSR (maximum 1, red color scale; bottom) of neurons in L_{INPUT}-L3 pair in each model. Red lines in L_{INPUT} are the input spike-timing sequences. Black dots are spikes in L3. (**D**) iSR-iFR profile of network model with FFI:FBI ratio at 7:3 (pink). In vivo–recorded iSR-iFR profile in the control condition (black filled circles, black dashed line) are plotted together for comparison. (**E**) Euclidean similarity of iSR-iFR profiles between in vivo data in control condition and simulation of the network model with different ratio of FFI:FBI showing 7:3 as the optimal ratio for the synchronization of spike times. Different ratios of FFI:FBI color-coded as different shades of magenta to orange. (**F**) iSR-iFR profile in response to increase in synaptic weights of FFI ($\Delta W_{FFI} > 0$) complemented by decrease in synaptic weights of FBI ($\Delta W_{FBI} < 0$) in the network model to balance inhibition (filled magenta circle). ChR2-PV activation (blue filled circles, magenta dashed line), ChR2-SST activation (blue filled circles, orange dashed line), Arch-PV silencing (green filled circles, magenta dashed line), and Arch-SST silencing (green filled circles, orange dashed line) are plotted together for comparison. In vivo data represent means ± SEM. (**G** and **H**) Same as (B) and (C) but in a network model with $\Delta W_{FFI} > 0$ and $\Delta W_{FBI} < 0$ in the model. (**I**) Four-dimensional Euclidean similarity of iSR-iFR profiles between in silico model in (F) and in vivo data in each condition. Magenta bar, optogenetic manipulation of PV interneuron in vivo; orange bar, optogenetic manipulation of SST interneuron in vivo. Blue and green shades indicate ChR2 activation with blue light and Arch silencing with green light in each interneuron subtypes, respectively. (**J** to **M**) Same as (F) to (I) but with $\Delta W_{FBI} > 0$ complemented by $\Delta W_{FFI} < 0$ in the network model to balance inhibition. The corresponding iSR-iFR profile is shown in filled orange circles in (J). (**N**) Cartoon summarizing the frequency-selective gating of spike-timing synchronization by PV and SST interneurons through preferential activation of FFI and FBI.

iSR-iFR profiles in the model with increased W_{FBI} showed greater Euclidean similarity to the optical activation of ChR2-SST interneurons and optical silencing of Arch-PV interneurons (Fig. 4M). The same simulation repeated with modulating W_{FFI} or W_{FBI} without balancing the total amount of inhibition in the network could not replicate the in vivo results (fig. S9). Together, these results suggest that there is a balance between feedforward and feedback inhibition in S1, and our optical manipulations altered spike-timing synchronization by breaking this balance in a complementary and push-pull manner. Specifically, optical activation of ChR2-PV interneurons or optical silencing of Arch-SST interneurons may have promoted feedforward inhibition over feedback inhibition, while optical silencing of Arch-PV interneurons or optical activation of ChR2-SST interneurons may have promoted feedback inhibition over feedforward inhibition (Fig. 4N).

DISCUSSION

Combining single-unit recordings with optogenetic manipulations of PV and SST interneurons, we examined the contribution of inhibitory interneurons to the spatiotemporal synchronization of precise spike times in S1 between L4 and either L5 or L6. We found

that, on any given trial, some L5 and L6 neurons (which we dubbed synchronized neurons) responded to whisker stimulation with spike-timing sequences that replicated both the spike times and firing rates of L4 neurons (Fig. 1), showing synchronization across layers. Moreover, we showed that PV and SST interneurons make different contributions to the synchronization of spike times from L4 to L5 and L6. PV interneurons helped to synchronize spike times from L4 to L5 and L6 when the iFR is low (<12 Hz; Figs. 2K and 3K), whereas SST interneurons help to synchronize spike times when the iFR is high (>12 Hz; Figs. 2L and 3L). We then ran in silico simulations of three-layer spiking neural networks with different degrees of feedforward and feedback inhibition (Fig. 4). These simulations revealed that the impact of PV and SST manipulations on spatiotemporal spike-timing synchronization in vivo mirrored the impact of in silico manipulations of feedforward and feedback inhibition.

One of the most important, previously unidentified aspects of our study is the examination of how spike-timing synchronization depends on the iFR of L4 neurons (Figs. 1L; 2, K and L; and 3, K and L). If we had limited our analysis to the synchronization of spike times irrespective of their iFR, we would not have observed any differences between PV and SST interneurons. This result provides further evidence that, in vivo, spike times and firing rate cannot be considered in isolation (*5*, *6*). Therefore, we propose that future research into the communication of sensory information using spike times should incorporate iFR analyses.

By using both optogenetic activation and silencing of interneurons, we were able to demonstrate that PV and SST interneurons serve as firing rate–dependent filters on the synchronization of spike-timing sequences between L4 and L5/L6 (Figs. 2, K and L, and 3, K and L). Specifically, PV interneurons function as a low-pass filter, helping to synchronize spike times when firing rates are low, whereas SST interneurons function as a high-pass filter, helping to synchronize spike times when firing rates are high. On the corollary, our results could also be interpreted as activation of PV and SST interneurons promoting "desynchronization" of spike times at high and low iFRs, respectively, which is consistent with previous findings that activation of SST interneurons promotes desynchronization of cortical activity in vivo (*28*). Given our results, PV activation may reduce synchronization during active states of sensory processing, while SST activation may reduce synchronization in states of low arousal or during sustained sensory responses after some adaptation. Thus, it will be interesting to examine how these distinct interneuron classes modulate information communication via spike-timing synchronization/desynchronization during different brain states.

Optical activation of PV interneurons (Fig. 2K) and optical silencing of SST interneurons (Fig. 3L) had the same effect in synchronizing spike times at low iFR, and both could be explained by preferential recruitment of feedforward inhibition over feedback inhibition (Fig. 4, F to I). SST interneurons in L4 can directly inhibit PV interneurons (*13*, *29*); thus, silencing of SST interneurons could have enhanced the activity of subpopulations of PV interneurons (*29*). In addition, optical silencing of SST interneurons that preferentially inhibit excitatory neurons could have increased firing rates of excitatory neurons, which, in turn, may have increased the recruitment of PV interneurons (*29*). Therefore, silencing of SST interneurons and activation of PV interneurons could have occurred concurrently in synchronizing spike times at low iFR in vivo. Similarly, synchronizing spike times at high iFR could be explained by concurrent silencing of PV interneurons and activation of SST interneurons in vivo.

By using in vivo spike-timing sequences as input to our in silico model and comparing the simulated and real data, we found that our in vivo data can be explained if PV interneurons preferentially contribute to promoting feedforward inhibition over feedback inhibition, while SST interneurons preferentially contribute to promoting feedback inhibition over feedforward inhibition, which is unexpectedly consistent with in vitro and in vivo studies of these interneuron classes in S1 (*13*–*15*). Moreover, the low/high-pass filtering function of PV and SST interneurons in our study is also consistent with reports that feedforward inhibition filters high-frequency spikes (*30*, *31*), while feedback inhibition synchronizes spikes to gamma frequencies (*32*).

Our in silico model simulation revealed that simply increasing or decreasing W_{FFI} or W_{FBI} alone without balancing the inhibition in the network fails to replicate the effect of activation or silencing of PV or SST interneurons on spike-timing synchronization (fig. S9). That is, simply turning on or off the same neural circuit cannot explain our in vivo results. However, when the increase in W_{FFI} was complemented by a decrease in W_{FBI} (Fig. 4F) and vice versa (Fig. 4J) to balance the inhibition in the network in a push-pull manner, the in silico results matched the in vivo results (Fig. 4, I and M). These data suggest that a fine balance between feedforward and feedback inhibition exists, and optogenetic manipulations of PV and SST interneurons perturbed this balance in a complementary, push-pull manner. As both PV and SST interneurons provide not only feedback inhibition but also feedforward inhibition (*33*), the preferential recruitment of feedforward and feedback inhibition by optogenetic manipulations of PV and SST interneurons we observe here may arise from interactions of complex neural circuitry. Therefore, direct assignment of PV interneurons to feedforward circuits and SST interneurons to feedback circuits warrants caution.

There are several additional limitations to our study that should also be noted. First, differences in photo-addressability (*34*), connectivity, and distribution of PV and SST interneurons across layers (*13*) and how they are affected under different behavioral/modulatory states may complicate interpretations of their roles in spike-timing synchronization (*13*, *14*, *35*). While many in vivo behavior studies revealed that spike-timing synchronization is related to the behavioral context (*1*–*3*), our in vivo experiments are conducted under anesthesia. Recent findings showed that the activity of SST interneurons is different in awake and in anesthesia states (*14*). Thus, future studies will need to address our findings in the awake state. Nevertheless, our results from lightly anaesthetized animals may be of significance to neuronal processing and memory consolidation in sleep states. Second, the three-layer network model that we used here does not capture the intricate anatomical and physiological characteristics of the real S1, meaning all conclusions drawn from the model must be taken with some caution. Despite these shortcomings, we used the network model solely to examine the relative contributions of feedforward and feedback inhibition on the synchronization of spikes across layers, and this is a well-established modeling framework that is widely used in investigating the synchronization of different neural codes (*26*, *27*). Third, on the basis of the canonical microcircuit for the flow of sensory information in S1 (*17*), we focused our analyses on the synchronization of spike times between L4 and the subgranular layers, L5 and L6. However, many L5 neurons have spike latencies as short as L4 neurons, suggesting that primary thalamic information flows simultaneously to L4 and L5 (*18*). Therefore, the synchronization of sensory information and spike times via other routes deserves further investigation.

In summary, by combining single-unit recording, optogenetics, and computational modeling, we have shown that temporally precise spike times can be reliably synchronized from L4 to L5 and L6 during passive whisker stimulation in an anesthetized state in vivo. In addition, we have shown that such synchronization is dynamically gated by PV and SST interneurons by breaking the balance between feedforward and feedback inhibitory neural circuits to preferentially recruit distinct inhibitory motifs. Our results add to the repertoire of proposed functions of PV and SST interneurons and help to delineate their potential role in regulating sensory information processing across cortical laminae.

MATERIALS AND METHODS

Animals

All experimental procedures were approved by the Institutional Animal Care and Use Committee (IACUC) at Korea University (KUIACUC-2017-157, KUIACUC-2018-69, KUIACUC-2019-0068), and all experimental procedures at the University of Oxford involving animals were conducted in accordance with the UK Animals in Scientific Procedures Act (1986). We used three different lines of mice: C57BL/6 wild-type (Gyerim Experimental Animal Resource Center in Korea, Envigo in the United Kingdom), PV-Cre (JAX #017320, Jackson Laboratory), and SST-Cre (JAX #013044, Jackson Laboratory) mice of either sex. Mice were maintained in a temperature-controlled environment on a 12-hour/12-hour light/dark cycle. Food and water were provided ad libitum.

Virus and stereotaxic surgery

To optogenetically manipulate the spike activities of PV and SST interneurons (Figs. 2 and 3 and figs. S3 and S5 to S8) (*22*), we expressed blue light-gated cation channel (ChR2) and green-yellow light-gated H^+ transporter (Arch) (*25*) in these neuronal types by injecting either adeno-associated virus (rAAV) vectors AAV5-EF1a-DIO-hChR2(E123T/T159C)-mCherry [University of North Carolina at Chapel Hill (UNC) Vector Core] (*22*) or AAV5-EF1a-DIO-eArch3.0-EYFP (UNC Vector Core) (*25*) in PV-Cre mice (postnatal days 46 to 84) and SST-Cre mice (postnatal days 49 to 83). Mice were head-fixed into a stereotaxic device (51730; Stoelting Inc.) under deep isoflurane anesthesia, and viral solutions (500 to 600 nl; ChR2, 3.8×10^{12} virus molecules/ml; Arch, 5×10^{12} virus molecules/ml) were delivered to either the left or right barrel cortex [S1; anterior-posterior (AP), −1.3 mm; medial-lateral (ML), ±3.3 mm from bregma]. Injections were made at two cortical depths (300 and 600 μm depth from pia) using either a 5-μl syringe connected to a motorized stereotaxic injector (The Stoelting Quintessential Injector, 53311, Stoelting Inc.) or a beveled injection pipette connected to a nanoliter injector (Nanoject II, Drummond Scientific) at a speed of 50 to 150 nl/min. The injection needle was left in the brain for more than 5 min following injection to prevent withdrawal of virus. At least 2 weeks of recovery time was allowed after the surgery before conducting in vivo recordings.

In vivo recordings and optogenetic light stimulation

Mice were head-fixed into a stereotaxic device (51730; Stoelting Inc.) under anesthesia [ketamine (75 to 100 mg/kg) and medetomidine (1 mg/kg)]. In vivo single-unit recordings were made by implanting a 32-channel silicon probe (A1×32-poly2-5mm-50s-177-OA32, A1×32-5mm-25-177-A32; NeuroNexus; Fig. 1, A and B, and fig. S1) into S1 on either left or right hemisphere (AP, −1.3 mm; ML, ±3.3 mm from bregma; 800 to 950 μm depth from the pia) during stimulation of whiskers on the contralateral side of the electrode implant. Whiskers were glued together and inserted into a capillary tube attached to a piezoelectric bimorph actuator (E650.00 LVPZD amplifier, Physik Instrumente) or motorized actuator, which was controlled by custom-made pulse generator based on Arduino and stimulated sinusoidally at 12 Hz for 3 s (Fig. 1A). Recordings of whisker stimulation–evoked responses were repeated 40 times with an intertrial interval of 10 s. Body temperature was monitored and maintained at 37°C using a DC temperature control system (40-90-8D, FHC Inc.) throughout all experiments. Signals were sampled at 25 kHz (RZ2 system, Tucker-Davis Technologies) or 30 kHz (RHD2000, Intan Technologies).

Blue light (473 nm) diode laser (iBeam smart 473, TOPTICA Photonics) was used to activate ChR2-PV and ChR2-SST interneurons (Fig. 2 and figs. S3 and S5 to S8), and green light (565 nm) light-emitting diode (LED) (M565F3 with LEDD1B, Thorlabs) was used to silence Arch-PV and Arch-SST interneurons (Fig. 3 and figs. S3 and S5 to S8). Light was delivered through an optical fiber [diameter, 200 μm; 0.22 numerical aperture (NA); FG200UCC; Thorlabs] placed on the cortical surface <500 μm from the recording site for green light LED or through an optic fiber, which was laminated on the 32-channel optrodes for blue light laser and green light LED (A1×32-poly2-5mm-50s-177-OA32; NeuroNexus). To prevent light stimulation–evoked artifacts, light stimulation preceded the onset of whisker stimulation by 500 ms (Figs. 2, E and F, and 3, E and F). Optogenetic activation of ChR2-PV and ChR2-SST interneurons could shut down spike activities of excitatory neurons, while optogenetic silencing of Arch-PV and Arch-SST interneurons could induce epileptic spike activity in excitatory neurons. In addition, it is difficult to precisely replicate how light affects opsins across different animals. Therefore, we aimed to obtain data using a range of light intensities that would optogenetically manipulate PV and SST interneurons activity while not causing abovementioned extreme effects on the putative excitatory neuron firing rates. Hence, we measured the firing rates of putative excitatory neurons during whisker stimulation combined with four different light stimulation intensities of blue laser (7.76, 39.47, 78.52, and 153.85 mW/mm^2) (fig. S5, A to D) and green LED (2.67, 5.05, 19.07, and 31.18 mW/mm^2) (fig. S5, E to H). We show that three different intensities of blue laser (7.76, 39.47, and 78.52 mW/mm^2) and green LED (2.67, 5.05, and 19.07 mW/mm^2) had minimal effect on the overall network activity as shown by negligible modulation of excitatory neuron firing rates (SD in PV-Cre mice with blue laser = 6.30%; SST-Cre mice with blue laser = 6.86%; PV-Cre mice with green LED = 6.35%; SST-Cre mice with green LED = 6.31%) (fig. S5). Different light stimulation intensities were counterbalanced and randomly interleaved during experiments, but due to restrictions on the recording session duration, some of the experiments could only be carried out with one or two light stimulation intensities. The effects of blue and green light stimulation to ChR2-PV and Arch-PV and SST interneurons in subgranular layers (L5 and L6), respectively, were confirmed by their firing rate changes upon light stimulation (fig. S6). To directly test the effect of different levels of light stimulation intensities for optogenetic PV and SST interneuron manipulations on iSR-iFR profiles, we analyzed data that included all three different light stimulation intensities in single recording trials (fig. S7). To further test whether different levels of perturbations in excitatory neurons' activity caused by optogenetic modulation of PV/SST interneurons

had any impact on the iSR-iFR profiles, we categorized the different perturbation levels by calculating the change in firing rate of L5/L6 excitatory neurons before and during optical manipulation ($FR_{light\ on}/FR_{light\ off}$; fig. S8). Experiments were sorted in three different bins based on the $FR_{light\ on}/FR_{light\ off}$ values of L5/L6 excitatory neurons. For optogenetic activation of ChR2-PV and ChR2-SST interneurons using blue light stimulation intensities (7.76 to 153.85 mW/mm^2), $FR_{light\ on}/FR_{light\ off}$ was binned into 0 to 0.4, 0.4 to 0.7, and 0.7 to 1.0 (fig. S8), while, for optogenetic silencing of Arch-PV and Arch-SST interneurons using green light stimulation intensities (2.69 to 31.18 mW/mm^2), $FR_{light\ on}/FR_{light\ off}$ was binned into 1.0 to 1.4, 1.4 to 1.7, and 1.7 to 2.0 (fig. S8).

Immunohistochemistry

Following in vivo recordings, mice were decapitated and their brains were fixed overnight in 4% paraformaldehyde in phosphate-buffered saline (PBS; Sigma-Aldrich). Brains were then washed in PBS before being cryoprotected overnight in 10% sucrose in PBS. Tissues were frozen in dry ice, and 50-μm coronal cryosections were made around the injection site in S1. The fluorescent tags of the ChR2 and Arch opsins, mCherry and EYFP, respectively, were boosted by counterstaining for the tag. Slices were washed with PBS and incubated for 2 hours in blocking solution (0.1 M PBS, 0.25% Triton X-100, and 5% normal goat serum; Sigma-Aldrich). Tissue was treated with primary antibody, rabbit anti-dsRed (Takara Bio) 1:500, or chicken anti-GFP (green fluorescent protein) (Abcam) 1:1000, overnight at 4°C in blocking solution. After washing in PBS, slices were stained with secondary antibody, goat anti-rabbit Alexa Fluor 568 (Life Technologies), or goat anti-chicken Alexa Fluor 488 (Abcam), 1:1000, for 2 hours at room temperature. Tissue was washed in PBS before counterstaining with 4′,6-diamidino-2-phenylindole (DAPI; Thermo Fisher Scientific) and mounting, with the slides sealed using nail polish. Images were acquired using confocal microscopy (Figs. 1B, 2B, and 3B; LSM880, Zeiss).

Analysis of in vivo electrophysiology data

All data were analyzed offline using custom-written codes in MATLAB (R2017a). To determine the laminar location of each single-unit (Fig. 1B), we estimated the cortical depth of the individual channels using the CSD depth profiles from local field potentials (LFPs; fig. S1). LFPs were analyzed by down-sampling the raw signals to 1 kHz and band-pass filtering them at 0.5 to 300 Hz. We averaged LFP recordings during whisker stimulations and applied spatial smoothing and secondary derivation on the averaged LFP by following equations to analyze CSD depth profile

$$\underline{\phi}(r) = \frac{1}{4}\left(\phi(r+h) + 2\phi(r) + \phi(r-h)\right)$$

$$\mathrm{CSD} = \frac{1}{h^2}\left(\underline{\phi}(r+h) - 2\underline{\phi}(r) + \underline{\phi}(r-h)\right)$$

where $\phi(r)$ is LFP at depth r and h is the depth interval. Positive value corresponds to sources and negative value corresponds to sinks in the CSD depth profiles (fig. S1). L4 was identified as early sink in upper layer, and L5B was identified as early sink in lower layer (fig. S1).

To obtain single-unit spike activities from the in vivo–recorded raw signals (Fig. 2C), raw signals were band-pass–filtered (300 to 5000 Hz), after which spike detection and sorting were performed using Klusta-suite software (http://klusta.readthedocs.io). The spike threshold level was set to 4.5-fold of the SD of each recorded signal. To ensure the single-unit isolation quality, we inspected the shape of spike waveforms, ISIs, and the shape of the autocorrelogram of spike times. We only included units showing clear negative deflection in the spike waveform, from which spike waveforms −0.5 to +1.0 ms relative to the spike peak were extracted. In addition, units with ISIs not violating the refractory period of neurons (2 ms) were considered as a single unit. We calculated autocorrelogram of spikes using the following equation

$$C_i(\tau) = \sum_{i \neq j} \delta\left(\tau - (T_i - T_j)\right)$$

where $T_{i,j}$ is the spike times i and j, and we used units with clear refractory period.

We classified the neuronal types into putative excitatory neurons and inhibitory interneurons by calculating the initial baseline-to-peak amplitude (a; Fig. 1C), the last baseline-to-peak amplitude (b; Fig. 1C), the spike width (c; Fig. 1C), and the asymmetry index ($[(b - a)/(b + a)]$) from the spike waveform (Fig. 1C). Neurons that were located on the right side of the decision boundary ($[(b - a)/(b + a)] = 2 * c - 0.6$; Fig. 1C) were considered putative excitatory neurons, while those on the left side of the decision boundary were considered putative interneurons. These putative excitatory neurons were further classified into whisker stimulation–responsive excitatory neurons when their firing rates during whisker stimulation increased more than twofold of SD of firing rate 1 s before whisker stimulation (Fig. 1D). PSTH was computed by averaging spike times relative to whisker stimulation for each trial using 100-ms time bin. Only putative excitatory neurons that were classified as whisker stimulation–responsive were used for further analysis.

Analysis of the synchronization of precise spike times

To identify the first cortical layer that responds to whisker stimulation, we analyzed the peak latency of whisker stimulation–evoked MUA in each layer. MUA was defined as the median spike times of all neurons in each layer within a 50-ms time window after whisker stimulation onset (Fig. 1E). Although there was no statistical difference between the peak MUA latencies in each layer, following the canonical flow of sensory information, we assumed L4 as input to S1.

To determine whether precise spike times and spike-timing sequences of units in L4 can synchronize to subgranular layers (L5 and L6 of S1), we calculated how similar spike times of L4 and that of other neurons in subgranular layers (Fig. 1F) and supragranular layers (L2/3; fig. S4) are using two different measures: spike-time coherence score and similarity (SR). Spike-time coherence score measures the degree of correlation between binarized spike-timing sequences (Fig. 1, G and H). We performed pairwise coherence analysis of L4 neuron and a neuron in another layer by taking the Fourier transform of the cross-covariance function of binarized (2-ms bin) spike-timing sequence [$s_x(t)$ and $s_y(t)$] and normalizing it by the Fourier transforms of the autocovariance function as follows

$$\mathrm{cov}_{xy}(\tau_c) = \left\langle \frac{1}{T}\sum_{t=1}^{T}(s_x(t) - \langle s_x(t)\rangle)\left(s_y(t+\tau) - \left\langle s_y(t+\tau)\right\rangle\right)\right\rangle$$

$$\mathrm{coh}_{xy}(\tau_c) = i\mathrm{FFT}\left(\frac{\mathrm{cov}_{xy}(\omega)}{\sqrt{\mathrm{cov}_{xx}(\omega) \times \mathrm{cov}_{yy}(\omega)}}\right)$$

where < > is expected values, T is the total duration of $s_x(t)$, τ_c is time lag, and cov(ω) is Fourier transform of cov(τ) (*36*). To reliably find precise synchronization of spike times evoked by whisker stimulation across the layers within cortical column, peak coherence within a narrow time window (-10 ms $< \tau_c <$ 10 ms) showing whisker stimulation–evoked columnar responses was used as coherence value for further analysis. After calculating spike-time coherence score of each pair of neurons, we analyzed the probability distribution of spike-time coherence scores and its multimodality was tested by Silverman's unimodal test (Figs. 1H; 2, G and H; and 3, G and H). If the distribution of spike-time coherence was not statistically unimodal, we fit a mixture of two log-normal distributions to spike-time coherence distribution using the expectation-maximization algorithm. The intersection of the two log-normal distributions was defined as the empirically determined "threshold" (Figs. 1H; 2, G and H; and 3, G and H and figs. S2C and S4C) that helped us classify the neurons into two groups: synchronized neuron and nonsynchronized neuron (Fig. 1I). The statistical differences between the distributions of spike-time coherence scores between layers and experiment conditions (Figs. 1H; 2, G and H; and 3, G and H and figs. S2C and S4C) were compared using two-sample Kolmogorov-Smirnov test. The coherence analysis was performed in 1-s-long time window that slid in 10-ms steps across the 3-s-long whisker stimulation–evoked spike-timing sequence, and the 1-s-long spike-timing sequences showing maximum coherence were used for further analysis.

To investigate whether there is a trial-to-trial variability in the role of a given neuron in synchronizing or nonsynchronizing spike times, we counted the number of switches made over trials of a nonsynchronized neuron to synchronized neuron or vice versa (fig. S3, A to C). We calculated the probability of switch as dividing the number of switches by the total number of trials (fig. S3D).

To further analyze whether the precise spike times of L4 could synchronize to synchronized neurons in the subgranular layers in a given trial, we used a measure called SR, which quantifies spike-timing synchronization of two spike trains (*20*). SR was calculated by normalizing the number of quasi-simultaneous spike times between two spike-timing sequences using the following equations

$$\mathrm{SR} = \frac{c(y|x)+c(x|y)}{M_x M_y}, c(x|y) = \sum_{i=1}^{M_x}\sum_{j=1}^{M_y} J_{ij}, J_{ij} = \begin{cases} 1 \; if \; -\tau < s_i^x - s_j^y < \tau \\ \frac{1}{2} if s_i^x = s_j^y \\ 0 \; \text{else} \end{cases}$$

where τ is the maximal synaptic time delay (20 ms), $M_{x,y}$ is the number of spikes for spike-timing sequence x and y, and $s_{\{i,j\}}^{\{x,y\}a}$ is spike times of ith or jth spike-timing sequence x or y. SR ranged from 0 to 1, where 0 means that two spike-timing sequences have no simultaneous spike times and 1 means that two spike times are identical within a synchronization timing window (±10 ms), which is an upper limit of within-column activity (*16*). To capture the transient, instantaneously changing characteristics of spike-timing sequence, we introduced a new measure we termed iSR, which quantifies SR within the ISIs of two consecutive spike-timing sequences of L4 (Fig. 1K) as follows

$$\mathrm{iSR}(t) = \mathrm{SR}([T_p^x(t), T_f^y(t)], [T_i^x(t) \ldots T_j^y(t)])$$

$$T_p^x(t) = (T^x \le t), T_f^x(t) = (T^x > t)$$

$$T_{i\ldots j}^y(t) = T^y \mid T^y \ge T_p^x(t) \,\&\, T^y < T_f^x(t)$$

where SR(x, y) is SR calculation for spike-timing sequence x and y, $T^{x,y}$ is spike times of x or y, T_p^x is the previous spike at time t, T_f^x is the following spike at time t of spike-timing sequence x, and $T_{i\ldots j}^y$ is the subset spike times of spike-timing sequence of y within T_p^x and T_f^x.

The transient iFR [iFR(t)] was analyzed by taking the reciprocal of ISIs. iFR(t) was categorized into four distinct frequency ranges (0.5 to 4, 4 to 12, 12 to 20, and 20 to 50 Hz; Figs. 1J; 2, I and J; and 3, I and J; and figs. S2D and S4D). To quantitatively characterize the frequency-dependent synchronization of whisker stimulation–evoked spike-timing sequence, we plotted iSR(t) as a function of iFR(t), which we termed "iSR-iFR profile" (Figs. 1L; 2, K and L; and 3, K and L; and figs. 2E, S4E, S7, S8, and S9).

To test whether the synchronization of precise spike times we observed with the whisker stimulation–evoked spikes is a biological phenomenon that occurs above chance level, we generated two surrogate datasets by shuffling the ISIs of whisker stimulation–evoked spikes recorded in vivo (fig. S2, A to C, top) and generating spike-timing sequences through Poisson-distributed random process (fig. S2, A to C, bottom). For shuffling the ISIs, we generated a random sequence of ISIs by keeping the first spike time and the number of spikes. For the Poisson-distributed random process, we generated random spike times while keeping the number of spikes the same.

Simulation of computational network model

We computationally modeled a three-layer network model composed of excitatory and inhibitory neurons. Each layer was composed of 200 excitatory neurons and 50 inhibitory interneurons (Fig. 4A and fig. S9A), reflecting the fact that interneurons comprise 20 to 25% of cortical neurons (*17*). Excitatory neurons and inhibitory interneurons were modeled as a single compartment conductance-based Hodgkin-Huxley neuron model (*37*). Membrane potential of excitatory neuron [$V_{m,\mathrm{EX}}(t)$] and inhibitory interneuron [$V_{m,\mathrm{IN}(t)}$] are described by the following equations

$$C_\mathrm{m}\frac{dV_{\mathrm{m,EX}}(t)}{dt} = -(I_\mathrm{Leak} + I_\mathrm{Na} + I_\mathrm{KDR} + I_\mathrm{KM})$$

$$C_\mathrm{m}\frac{dV_{\mathrm{m,IN}(t)}}{dt} = -(I_\mathrm{Leak} + I_\mathrm{Na} + I_\mathrm{KDR})$$

where C_m is the membrane capacitance, I_Leak is the leak, I_Na is the fast sodium channel current, I_KDR is the delayed rectifier potassium channel, and I_KM is the M-type potassium channel current (*31*). The parameters used for excitatory neurons and inhibitory interneurons are shown in Table 1.

Each excitatory neuron within a layer was modeled to receive excitatory synaptic inputs from randomly chosen excitatory neurons in the previous layer with connectivity probability of 10% (Fig. 4A and fig. S9A), reflecting the fact that cortical neurons have 10% connectivity (*38*). Each excitatory neuron was modeled to receive equal number of excitatory inputs and inhibitory inputs to balance excitation and inhibition of the network, similar to in vivo observations from cortical neural network (*11*). For the excitatory and inhibitory synapses, double-exponential conductance model was used with the following equation

$$I_\mathrm{syn}(t) = g_\mathrm{syn} * \mathrm{factor} * (e^{-t/\tau_\mathrm{decay}} - e^{-t/\tau_\mathrm{rise}}) * (V_\mathrm{m} - E_\mathrm{rev})$$

Table 1. Membrane properties in the Hodgkin-Huxley type excitatory neuron and inhibitory interneuron model.

Cell type	Excitatory neuron	Inhibitory interneuron
Diameter and length (μm)	70	40
Capacitance (μF/cm^2)	1.0	1.0
Membrane resistance (ohm·cm^2)	23,000	6,000
Axial resistance (ohm·cm)	50	50
Maximal conductance of I_{Leak} (g_{Leak}, S/cm^2)	0.0000438	0.000167
g_{Na} (S/cm^2)	0.012	0.015
g_{KDR} (S/cm^2)	0.0015	0.004
g_{KM} (S/cm^2)	0.000005	–

Table 2. Synapse model properties between excitatory neurons and inhibitory interneurons.

Synapses (presynaptic neuron–postsynaptic neuron)	Excitatory neuron–excitatory neuron	Excitatory neuron–inhibitory neuron	Inhibitory neuron–excitatory neuron
Maximal conductance (g_{syn}, μS)	0.0074	0.0012	0.00743
Rise time constant (τ_{rise}, ms)	0.1	0.2	1.0
Decay time constant (τ_{decay}, ms)	0.2	0.3	4.5
Reversal potential of synapse (E_{rev}, mV)	0	0	−70

where g_{syn} is the maximal conductance of synapse, factor is the normalizing constant, τ_{decay} is the decay time constant, τ_{rise} is the rise time constant, V_m is the membrane potential, and E_{rev} is the reversal potential of the synapse model. Each parameter was chosen to satisfy the unitary postsynaptic potentials observed in vitro (Table 2) (*39*).

To investigate the role of inhibitory circuit motifs in the synchronization of precise spike times, a three-layer network model with inhibitory interneurons that provides both feedforward and feedback inhibition at different ratios was constructed (Fig. 4A and fig. S9A). Feedforward inhibition was modeled such that interneurons received shared afferent excitatory inputs from excitatory neurons from the previous layer. Feedback inhibition was modeled such that interneuron received excitatory inputs from the excitatory neurons within the same layer, which, in turn, recurrently inhibited the excitatory neurons.

We modeled sparse representation of sensory information in cortical neurons (*19*) by giving in vivo spike-timing sequence recorded from L4 during whisker stimulation (Fig. 1) as input to only 40 excitatory neurons in the input layer (L_{INPUT}) of the network model, while the remaining 160 excitatory neurons were modeled to spontaneously spike with Poisson-randomized spike times with log-normally distributed firing rates ($\mu = 3.5$, $\sigma = 2.5$) as observed in vivo (Fig. 4, B, G, and K) (*40*).

To infer which inhibitory circuit motif is mediated by PV and SST interneurons, we treated iSR-iFR profile as four-dimensional Euclidean vector and compared the vectors of in vivo data and simulation data by calculating Euclidean similarity (Fig. 4, E, I, and M; and fig. S9, C and E) using the following equation

$$\text{Euclidean similarity} = \frac{1}{(1 + d(A,B))}$$

$$d(A,B) = \sqrt{\sum_{i=1}^{4} (A_i - B_i)^4}$$

All simulations were conducted with a sampling rate of 5 kHz in the NEURON simulation environment (https://neuron.yale.edu) and were repeated 20 times.

Statistical analysis

All values were represented as means ± SEM, where "*n*" refers to the number of pairs of spike-timing sequences between units in L4 and L5/6 (Figs. 1H; 2, G and H; and 3, G and H; and figs. S2C and S4C) or number of single units (Figs. 1L; 2, K and L; and 3, K and L; and figs. S2E; S4E; S5, B to H; S7; and S8) from in vivo recordings. For determining statistical significance of iSR-iFR profiles between synchronized and nonsynchronized neurons, we used Wilcoxon rank sum test showing the significance of iSR at each iFR frequency (Figs. 1L; 2, K and L; and 3, K and L). For the statistical difference of iSR between iFR bands, we used one-way ANOVA test (Fig. 1L). For the comparison of coherence distribution, we used Kolmogorov-Smirnov test. The statistical differences between iSR-iFR profiles in response to optogenetic manipulations of PV and SST interneurons using different light stimulation intensities and perturbation levels were tested using two-way ANOVA test (fig. S7 and S8). *P* values of less than 0.05 were deemed statistically significant.

SUPPLEMENTARY MATERIALS

Supplementary material for this article is available at http://advances.sciencemag.org/cgi/content/full/6/17/eaay5333/DC1

View/request a protocol for this paper from *Bio-protocol*.

REFERENCES AND NOTES

1. A. Riehle, S. Grun, M. Diesmann, A. Aertsen, Spike synchronization and rate modulation differentially involved in motor cortical function. *Science* **278**, 1950–1953 (1997).
2. A. Jackson, V. J. Gee, S. N. Baker, R. N. Lemon, Synchrony between neurons with similar muscle fields in monkey motor cortex. *Neuron* **38**, 115–125 (2003).
3. J.-e. Miller, I. Ayzenshtat, L. Carrillo-Reid, R. Yuste, Visual stimuli recruit intrinsically generated cortical ensembles. *Proc. Natl. Acad. Sci. U.S.A.* **111**, E4053–E4061 (2014).
4. A. J. Peters, S. X. Chen, T. Komiyama, Emergence of reproducible spatiotemporal activity during motor learning. *Nature* **510**, 263–267 (2014).
5. J. Biederlack, M. Castelo-Branco, S. Neuenschwander, D. W. Wheeler, W. Singer, D. Nikolić, Brightness induction: Rate enhancement and neuronal synchronization as complementary codes. *Neuron* **52**, 1073–1083 (2006).
6. Y. Zuo, H. Safaai, G. Notaro, A. Mazzoni, S. Panzeri, M. E. Diamond, Complementary contributions of spike timing and spike rate to perceptual decisions in rat S1 and S2 cortex. *Curr. Biol.* **25**, 357–363 (2015).
7. E. Salinas, T. J. Sejnowski, Impact of correlated synaptic input on output firing rate and variability in simple neuronal models. *J. Neurosci.* **20**, 6193–6209 (2000).
8. J. W. Middleton, C. Omar, B. Doiron, D. J. Simons, Neural correlation is stimulus modulated by feedforward inhibitory circuitry. *J. Neurosci.* **32**, 506–518 (2012).
9. S. Moldakarimov, M. Bazhenov, T. J. Sejnowski, Feedback stabilizes propagation of synchronous spiking in cortical neural networks. *Proc. Natl. Acad. Sci. U.S.A.* **112**, 2545–2550 (2015).

10. S. J. Cruikshank, T. J. Lewis, B. W. Connors, Synaptic basis for intense thalamocortical activation of feedforward inhibitory cells in neocortex. *Nat. Neurosci.* **10**, 462–468 (2007).
11. M. Wehr, A. M. Zador, Balanced inhibition underlies tuning and sharpens spike timing in auditory cortex. *Nature* **426**, 442–446 (2003).
12. Y. Shu, A. Hasenstaub, D. A. McCormick, Turning on and off recurrent balanced cortical activity. *Nature* **423**, 288–293 (2003).
13. R. Tremblay, S. Lee, B. Rudy, GABAergic interneurons in the neocortex: From cellular properties to circuits. *Neuron* **91**, 260–292 (2016).
14. H. Adesnik, W. Bruns, H. Taniguchi, Z. J. Huang, M. Scanziani, A neural circuit for spatial summation in visual cortex. *Nature* **490**, 226–231 (2012).
15. X. Xu, E. M. Callaway, Laminar specificity of functional input to distinct types of inhibitory cortical neurons. *J. Neurosci.* **29**, 70–85 (2009).
16. C. P. J. De Kock, R. M. Bruno, H. Spors, B. Sakmann, Layer- and cell-type-specific suprathreshold stimulus representation in rat primary somatosensory cortex. *J. Physiol.* **581**, 139–154 (2007).
17. R. J. Douglas, K. A. C. Martin, Neuronal circuits of the neocortex. *Annu. Rev. Neurosci.* **27**, 419–451 (2004).
18. C. M. Constantinople, R. M. Bruno, Deep cortical layers are activated directly by thalamus. *Science* **340**, 1591–1594 (2013).
19. A. L. Barth, J. F. A. Poulet, Experimental evidence for sparse firing in the neocortex. *Trends Neurosci.* **35**, 345–355 (2012).
20. R. Quian Quiroga, T. Kreuz, P. Grassberger, Event synchronization: A simple and fast method to measure synchronicity and time delay patterns. *Phys. Rev. E Stat. Nonlin. Soft Matter Phys.* **66**, 041904 (2002).
21. G. Buzsáki, A. Draguhn, Neuronal oscillations in cortical networks. *Science* **304**, 1926–1929 (2004).
22. A. Berndt, P. Schoenenberger, J. Mattis, K. M. Tye, K. Deisseroth, P. Hegemann, T. G. Oertner, High-efficiency channelrhodopsins for fast neuronal stimulation at low light levels. *Proc. Natl. Acad. Sci. U.S.A.* **108**, 7595–7600 (2011).
23. B. A. Seybold, E. A. K. Phillips, C. E. Schreiner, A. R. Hasenstaub, Inhibitory actions unified by network integration. *Neuron* **87**, 1181–1192 (2015).
24. S.-H. Lee, A. C. Kwan, Y. Dan, Interneuron subtypes and orientation tuning. *Nature* **508**, E1–E2 (2014).
25. J. Mattis, K. M. Tye, E. A. Ferenczi, C. Ramakrishnan, D. J. O'Shea, R. Prakash, L. A. Gunaydin, M. Hyun, L. E. Fenno, V. Gradinaru, O. Yizhar, K. Deisseroth, Principles for applying optogenetic tools derived from direct comparative analysis of microbial opsins. *Nat. Methods* **9**, 159–172 (2011).
26. M. Diesmann, M.-O. Gewaltig, A. Aertsen, Stable propagation of synchronous spiking in cortical neural networks. *Nature* **402**, 529–533 (1999).
27. A. Kumar, S. Rotter, A. Aertsen, Conditions for propagating synchronous spiking and asynchronous firing rates in a cortical network model. *J. Neurosci.* **28**, 5268–5280 (2008).
28. N. Chen, H. Sugihara, M. Sur, An acetylcholine-activated microcircuit drives temporal dynamics of cortical activity. *Nat. Neurosci.* **18**, 892–902 (2015).
29. H. Xu, H.-Y. Jeong, R. Tremblay, B. Rudy, Neocortical somatostatin-expressing GABAergic interneurons disinhibit the thalamorecipient layer 4. *Neuron* **77**, 155–167 (2013).
30. V. A. Klyachko, C. F. Stevens, Excitatory and feed-forward inhibitory hippocampal synapses work synergistically as an adaptive filter of natural spike trains. *PLOS Biol.* **4**, e207 (2006).
31. H. J. Jang, K. Park, J. Lee, H. Kim, K. H. Han, J. Kwag, $GABA_A$ receptor-mediated feedforward and feedback inhibition differentially modulate the gain and the neural code transformation in hippocampal CA1 pyramidal cells. *Neuropharmacology* **99**, 177–186 (2015).
32. S. R. Cobb, E. H. Buhl, K. Halasy, O. Paulsen, P. Somogyi, Synchronization of neuronal activity in hippocampus by individual GABAergic interneurons. *Nature* **378**, 75–78 (1995).
33. A. Naka, J. Veit, B. Shababo, R. K. Chance, D. Risso, D. Stafford, B. Snyder, A. Egladyous, D. Chu, S. Sridharan, D. P. Mossing, L. Paninski, J. Ngai, H. Adesnik, Complementary networks of cortical somatostatin interneurons enforce layer specific control. *eLife* **8**, e43696 (2019).
34. J.-W. Yang, P.-H. Prouvot, V. Reyes-Puerta, M. C. Stüttgen, A. Stroh, H. J. Luhmann, Optogenetic modulation of a minor fraction of parvalbumin-positive interneurons specifically affects spatiotemporal dynamics of spontaneous and sensory-evoked activity in mouse somatosensory cortex in vivo. *Cereb. Cortex* **27**, 5784–5803 (2017).
35. W. Muñoz, R. Tremblay, D. Levenstein, B. Rudy, Layer-specific modulation of neocortical dendritic inhibition during active wakefulness. *Science* **355**, 954–959 (2017).
36. R. R. Kimpo, F. E. Theunissen, A. J. Doupe, Propagation of correlated activity through multiple stages of a neural circuit. *J. Neurosci.* **23**, 5750–5761 (2003).
37. A. L. Hodgkin, A. F. Huxley, A quantitative description of membrane current and its application to conduction and excitation in nerve. *J. Physiol.* **117**, 500–544 (1952).
38. H. Markram, J. Lübke, M. Frotscher, A. Roth, B. Sakmann, Physiology and anatomy of synaptic connections between thick tufted pyramidal neurones in the developing rat neocortex. *J. Physiol.* **500** (Pt. 2), 409–440 (1997).
39. A. M. Thomson, D. C. West, Y. Wang, A. P. Bannister, Synaptic connections and small circuits involving excitatory and inhibitory neurons in layers 2-5 of adult rat and cat neocortex: Triple intracellular recordings and biocytin labelling in vitro. *Cereb. Cortex* **12**, 936–953 (2002).
40. G. Buzsáki, K. Mizuseki, The log-dynamic brain: How skewed distributions affect network operations. *Nat. Rev. Neurosci.* **15**, 264–278 (2014).

Acknowledgments

Funding: This work was supported by the Human Frontiers Science Program (HFSP) Young Investigator Award (RGY0073/2015) to B.A.R., M.M.K., and J.K. and by the National Research Foundation of Korea (NRF-2019M3E5D2A01058328) to J.K. H.J.J. was supported by a Korea University grant. J.M.R. was supported by a Wellcome Trust Prize Studentship. **Author contributions:** H.J.J., B.A.R., M.M.K., and J.K. conceived and designed the in vivo study. H.J.J., M.M.K., H.C., and J.M.R. performed in vivo experiments. H.J.J. and H.C. analyzed the in vivo data. H.J.J. and J.K. designed the network model. H.J.J. performed the simulations and analysis. J.M.R. and M.M.K. performed immunohistochemistry. H.J.J. and J.K. wrote the original draft. H.J.J., B.A.R., M.M.K., and J.K. reviewed and edited the manuscript. **Competing interests:** The authors declare that they have no competing interests. **Data and materials availability:** Klusta-suite is an open source spike detection and sorting software downloadable at https://github.com/kwikteam/klusta. NEURON is an open source simulation software downloadable at https://neuron.yale.edu/neuron/. Custom-made MATLAB codes used for data analysis are available from the corresponding authors upon request. All other data needed to evaluate the conclusions in the paper are present in the paper and/or the Supplementary Materials.

Submitted 28 June 2019
Accepted 17 January 2020
Published 22 April 2020
10.1126/sciadv.aay5333

Citation: H. J. Jang, H. Chung, J. M. Rowland, B. A. Richards, M. M. Kohl, J. Kwag, Distinct roles of parvalbumin and somatostatin interneurons in gating the synchronization of spike times in the neocortex. *Sci. Adv.* **6**, eaay5333 (2020).